



HAL
open science

Nanoarchitectonics of Metal Atom Cluster-Based Building Blocks Applied to the Engineering of Photoelectrodes for Solar Cells

Tatiana Lappi, Stéphane Cordier, Yakov Gayfulin, Soraya Ababou-Girard, Fabien Grasset, Tetsuo Uchikoshi, Nikolay G. Naumov, Adèle Renaud

► **To cite this version:**

Tatiana Lappi, Stéphane Cordier, Yakov Gayfulin, Soraya Ababou-Girard, Fabien Grasset, et al.. Nanoarchitectonics of Metal Atom Cluster-Based Building Blocks Applied to the Engineering of Photoelectrodes for Solar Cells. Solar RRL, 2023, pp.2201037. 10.1002/solr.202201037 . hal-04011024

HAL Id: hal-04011024

<https://hal.science/hal-04011024>

Submitted on 22 Mar 2023

HAL is a multi-disciplinary open access archive for the deposit and dissemination of scientific research documents, whether they are published or not. The documents may come from teaching and research institutions in France or abroad, or from public or private research centers.

L'archive ouverte pluridisciplinaire **HAL**, est destinée au dépôt et à la diffusion de documents scientifiques de niveau recherche, publiés ou non, émanant des établissements d'enseignement et de recherche français ou étrangers, des laboratoires publics ou privés.



Distributed under a Creative Commons Attribution - NonCommercial - NoDerivatives 4.0 International License

Nanoarchitectonics of Metal Atom Cluster-Based Building Blocks Applied to the Engineering of Photoelectrodes for Solar Cells

Tatiana Lappi, Stéphane Cordier,* Yakov Gayfulin, Soraya Ababou-Girard, Fabien Grasset, Tetsuo Uchikoshi, Nikolay G. Naumov, and Adèle Renaud*

This study deals with the nanoarchitectonic concept applied to the design of photoelectrodes built on two types of cluster core building blocks, namely, $\{\text{Re}_6\text{S}_8^i\}$ and $\{\text{Re}_6\text{Se}_8^i\}$. The effect of the nature of the metal/ligand on photoinduced conductivity properties is thus investigated through an in-depth photoelectrochemical study and it is rationalized by the establishment of an energy diagram using a set of complementary optical (ultraviolet–vis–near infrared), electrochemical and spectroscopic (X-ray photoelectron spectroscopy) characterization techniques. The optical and electronic properties of $\{\text{Re}_6\text{Q}_8^i\}$ -based films ($\text{Q} = \text{S}$ or Se) are drastically dependent on the composition. The sulfide-based photoelectrodes exhibit ambipolar behavior with an n-type domination whereas the selenide-based photoelectrodes have a p-type semiconducting behavior. Such electronic properties can be exalted by increasing the interactions between the cluster building blocks by heating. The design of mixed $\{\text{Re}_6\text{Q}_8^i\}$ -based photoelectrodes combining the two n- $\{\text{Re}_6\text{S}_8^i\}$ and p- $\{\text{Re}_6\text{Se}_8^i\}$ cluster core-based building blocks is explored. The physical properties of the heterostructures can be tuned by controlling the $\{\text{Re}_6\text{S}_8^i\}:\{\text{Re}_6\text{Se}_8^i\}$ ratio and the interaction between the clusters. The creation of such nanoarchitectonic p–n junctions allows the optimization of the photocurrents generated by increasing the separated charge state lifetime that turns out to be attractive for solar cell applications.

1. Introduction

In recent years, a significant body of research highlights the prospects of using ambipolar materials or devices for different applications such as photovoltaics,^[1–3] memories or logic transistors,^[4–7] synaptic,^[8,9] sensing^[10,11] and light-emitting devices,^[7,12,13] or photoelectrochemical cells.^[1,2,14] Currently, widely used devices are based on unipolar materials, p- and n-type semiconductors, where the predominant conductive charges are holes or electrons, respectively. The charge transport dominated by a single type of charge carrier limits the scope of applications of unipolar semiconductors and the performances of devices. In turn, ambipolar analogs make it possible to achieve simultaneous generation and transport of electrons and holes, which promote simultaneous p- and n-type characteristics in one and the same material, as well as electronic devices based on such materials, that offer new perspectives in term of use and integration. The ability to combine in the

same material both photogeneration/light emission and carriers extraction or injection allows to design simpler device

T. Lappi, S. Cordier, F. Grasset, A. Renaud
CNRS
ISCR-UMR
Université Rennes
F-35000 Rennes, France
E-mail: Stephane.cordier@univ-rennes1.fr; adele.renaud@univ-rennes1.fr

T. Lappi, Y. Gayfulin, N. G. Naumov
Nikolaev Institute of Inorganic Chemistry
Siberian Branch of Russian Academy of Sciences
630090 Novosibirsk, Russia

 The ORCID identification number(s) for the author(s) of this article can be found under <https://doi.org/10.1002/solr.202201037>.

© 2023 The Authors. Solar RRL published by Wiley-VCH GmbH. This is an open access article under the terms of the Creative Commons Attribution-NonCommercial-NoDerivs License, which permits use and distribution in any medium, provided the original work is properly cited, the use is non-commercial and no modifications or adaptations are made.

DOI: 10.1002/solr.202201037

S. Ababou-Girard
CNRS
IPR-UMR 6251
Université Rennes
F-35000 Rennes, France

F. Grasset, T. Uchikoshi
Laboratory for Innovative Key Materials and Structures (LINK)
CNRS-Saint-Gobain-NIMS
IRL 3629
National Institute for Materials Science
Tsukuba 305-0044, Japan

T. Uchikoshi
Research Center for Functional Materials
National Institute for Materials Science (NIMS)
Tsukuba 305-0047, Japan

architectures by limiting the number of layers and interfaces that affect the manufacturing and the device performances. For now, the most common and studied representatives of ambipolar materials are perovskite halides,^[1,3] carbon nanotubes,^[15,16] graphene and 2D chalcogenides,^[4,6,17,18] and organic semiconductors.^[3,7,9,11,12] This family of materials has recently been completed by a new series of compounds, namely, the iodides containing molybdenum octahedral clusters and built on $\{Mo_6I_8\}$ cores.^[19] These iodides themselves belong to the larger family of compounds built on cluster-based complexes with the general formula $\{[M_6Q_8]L^a_6\}$ ($M = Mo, W$ and Re ; $Q =$ chalcogen and/or halogen; $L =$ halogen or organic or inorganic functional groups). Within the $\{[M_6Q_8]L^a_6\}$ cluster unit, the M_6 cluster is covalently bound to face-capping ligands (Q^i) to form a chemically robust $\{M_6Q^i_8\}$ cluster core. The $\{M_6Q^i_8\}$ core as formed is coordinated to six terminal ligands (L^a) stabilizing the entire $\{[M_6Q_8]L^a_6\}$ nanosized architecture. The $\{[M_6Q_8]L^a_6\}$ cluster units exhibit unique optical properties. They absorb continuously from UV to visible and upon excitation at any wavelength within this window, they phosphoresce over a broad band ranging from red to NIR. The nanosized $\{[M_6Q_8]L^a_6\}$ cluster units are particularly well suited for nanoarchitectonics as described earlier.^[20,21] According to Ariga,^[22] “the concept of nanoarchitectonics is supposed to involve the architecting of functional materials using nanoscale units based on the principles of nanotechnology”. Thereby in recent years, the design of nanomaterials and surfaces integrating octahedral cluster-based units as functional building blocks^[23–29] have become an intense field of research that nicely illustrates the concept of nanoarchitectonics.^[22] As nonexhaustive results, the functionalization of graphene oxides by such clusters leads to efficient composites for hydrogen evolution reaction and photoreduction of CO_2 .^[30–33] More recently, the design of photoelectrodes by electrophoretic deposition (EPD) of $\{[Mo_6I_8]I^a_4(H_2O)^a_2\}$ cluster-based units on fluorine tin oxide (FTO) was reported.^[19] In that frame, the ambipolar behaviors of the $Cs_2\{[Mo_6I_8]I^a_6\}$ solid-state precursor and those of photoelectrodes based on layers of $\{[Mo_6I_8]I^a_4(H_2O)^a_2\} \cdot xH_2O$ were evidenced using complementary steady-state and transient photoelectrochemical characterization techniques (chronopotentiometry, current–potential, and impedance curves under chopped or constant illumination). An all-solid-state solar cell integrating a layer of $\{[Mo_6I_8]I^a_4(H_2O)^a_2\} \cdot xH_2O$ as a solar light harvester was assembled in order to demonstrate the simultaneous photogeneration and transport of electrons and holes. This exceptional ambipolar behavior was attributed to the confinement of electrons in the nanometric $\{[Mo_6I_8]L^a_6\}$ ($L = I$ or I and H_2O) building blocks. The electronic molecular structure of the $\{[Mo_6I_8]L^a_6\}$ cluster unit was determined from complementary optical (UV–vis), spectroscopic (X-ray photoelectron spectroscopy (XPS)), and electrochemical (cyclic voltammetry and impedance) techniques. It is not disturbed by stacking effects in the solid-state or when deposited on surfaces. The electronic structure of the resulting layers of clusters can be related to that of the intrinsic inorganic semiconductors with a localization of the Fermi level that pins at the middle of the bandgap. This particular behavior that was first characterized for molybdenum iodides should be extended to other members of the $\{[M_6Q_8]L^a_6\}$ family. It would thus offer a wide variety of ambipolar materials with tunable optical and

electronic properties. Indeed, the physical properties of the $\{[M_6Q_8]L^a_6\}$ cluster units depend on the nature of the metal and those of inner and apical ligands as well as on the number of valence electrons available for metal bonding. The absorption and emission properties can be efficiently improved by combining the solid-state chemistry and solution chemistry. It gives rise to a wide range of $\{[M_6Q_8]L^a_6\}$ cluster units suitable for the design of hybrid materials and functional surfaces with tunable optical properties. In order to go deeper in the nanoarchitectonic concept of the design of photoelectrodes and to know more about the effect of the nature of the metal on photoinduced conductivity properties, the investigation was extended to the $\{Re_6Q^i_8\}$ cluster core-based sulfides and selenides. In this work, the engineering of photoelectrodes for solar cells based on two types of building blocks with similar geometrical features but with significantly different physical and chemical properties was explored. $\{[Re_6Se^i_8]Cl^a_6\}^{n-}$ and $\{[Re_6S^i_8]Cl^a_6\}^{n-}$ cluster-based units^[34–36] were selected and investigated as functional light-harvesting building blocks and as electron/hole pair generators. Despite similar sizes and geometrical features, owing to the lower electrophile character of selenium compared to sulfur, $\{[Re_6Se^i_8]Cl^a_6\}^{n-}$ and $\{[Re_6S^i_8]Cl^a_6\}^{n-}$ have different electronic structures and highest occupied molecular orbital (HOMO)/lowest unoccupied molecular orbital (LUMO) gaps leading to significant differences in physical properties.^[34–36] Among others, the $\{Re_6Se^i_8\}^{2+}$ selenide cluster core is less electrophile than the $\{Re_6S^i_8\}^{2+}$ sulfide, the quantum yields of emission and phosphorescence decay lifetimes are higher for $\{Re_6Se^i_8\}^{2+}$ selenides than for $\{[Re_6S^i_8]^{2+}$ sulfides, and the redox potential is higher for $\{Re_6S^i_8\}^{2+}$ than for $\{Re_6Se^i_8\}^{2+}$. Herein, $((n-C_4H_9)_4N)_3\{[Re_6S^i_8]Cl^a_6\}$ and $((n-C_4H_9)_4N)_3\{[Re_6Se^i_8]Cl^a_6\}$ ^[37–39] were used as precursors on the one hand to prepare by EPD process photoelectrodes based on $\{Re_6S^i_8\}$ and $\{Re_6Se^i_8\}$ cluster cores and on the other hand, to design composite photoelectrodes based on mixtures of $\{Re_6S^i_8\}$ and $\{Re_6Se^i_8\}$ cluster cores. Thus, the variation of electronic properties according to the composition was evidenced and led to original p–n junctions using various $\{Re_6S^i_8\}:\{Re_6Se^i_8\}$ ratios. In a perspective of integration in solar systems, the photoconversion performances of single $\{Re_6Q^i_8\}$ ($Q = S$ or Se)- and mixed $\{Re_6S^i_8\}:\{Re_6Se^i_8\}$ -based photoelectrodes were investigated using a similar set of photoelectrochemical characterizations used for $\{Mo_6I_8\}$ -based compounds previously reported.^[19]

2. Results and Discussion

2.1. Synthesis and Characterization of Cluster-Based films

Brown $\{Re_6Q^i_8\}$ ($Q = S$ or Se)-based films of thickness around 4 and 7 μm for $\{Re_6S_8\}$ - and $\{Re_6Se_8\}$ -based cluster cores respectively were obtained by EPD (Figure 1 and 2) by applying a constant voltage of 40 V for 30 s between electrodes immersed into the solution of $(Bu_4N)_3[Re_6Q^i_8Cl_6]$ in acetonitrile.

Due to their charge, tetrabutylammonium cations and $\{Re_6Q^i_8\}$ -based anions drift at the opposite electrodes during the EPD process. Thus, cluster-based amorphous layers (Figure S1, Supporting Information) with a composition slightly different from those of the cluster precursor powders were obtained on the anode side. The presence of $\{Re_6Q^i_8\}$

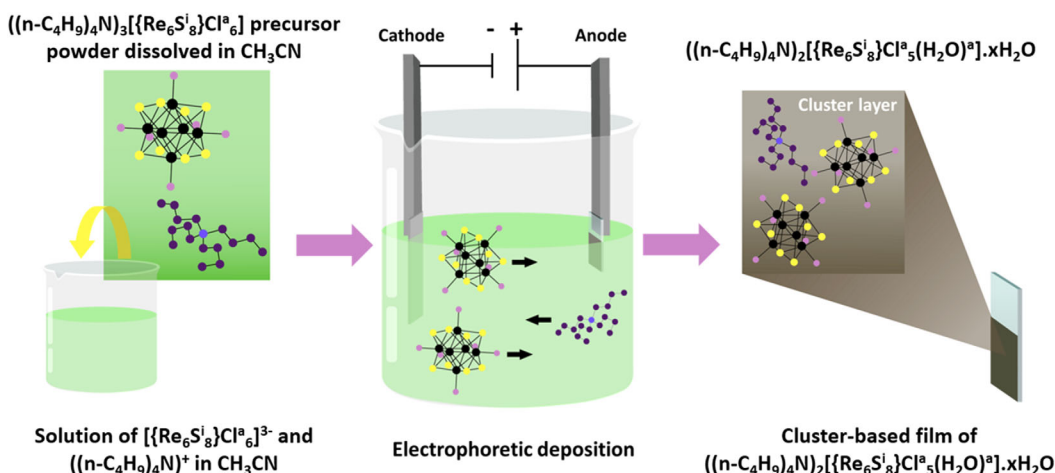


Figure 1. Schematic process of the deposition of the cluster building blocks from $\{Re_6S_i^i\}Cl_6^{3-}$ in the solid-state and in the starting solution to $\{Re_6S_i^i\}Cl_5(H_2O)^9$ after immobilization on FTO substrates by EPD method. The deposition process is the same for the $\{Re_6Se_i^i\}Cl_6$ -based building blocks.

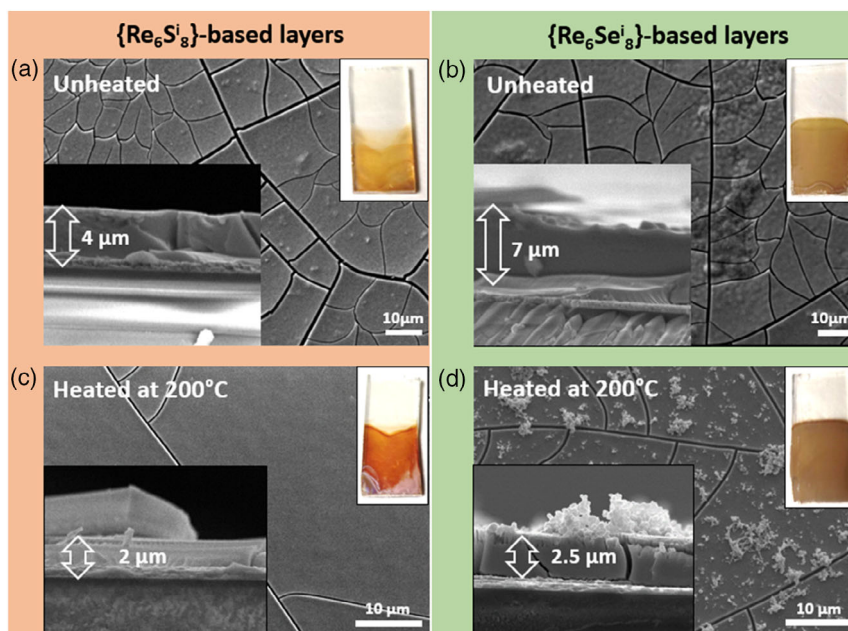


Figure 2. Scanning electron microscopy (SEM) images of a) unheated and c) heated at 200 °C $\{Re_6S_i^i\}$ -based films and b) unheated and d) heated at 200 °C $\{Re_6Se_i^i\}$ -based films.

(Q = S or Se) cluster cores in the films was confirmed by Raman spectroscopy. Raman bands (Figure S2, Supporting Information) of the spectra of the precursor powders and films are located at the same position for the sulfur and selenium homologues, respectively. The experimental positions are in good agreement with the vibration frequency values earlier determined by Hartree–Fock and by density functional theory calculations^[35] (224 cm^{-1} for $A_{1g} Cl_6$, 278 cm^{-1} for $A_{1g} Re_6$, 430 cm^{-1} for $A_{1g} S_8$, and 191 cm^{-1} for $A_{1g} Re_6$, 216 cm^{-1} for $A_{1g} Cl_6$, and 267 cm^{-1} for $A_{1g} Se_8$ for sulfur and selenide cluster complexes, respectively). The Raman bands recorded on the films are however broader. It is assigned to the loss of organization due the amorphous character of the layers or/and to the loss of symmetry due to the partial substitution of terminal ligands as discussed below.

This tendency is confirmed by XPS analyses. The chemical stability of the cluster cores and the partial substitution of terminal ligands were highlighted by XPS investigations (Figure 3, S3, and S4, Supporting Information and Table 1). Comparing XPS spectra of the precursor powder and those of the film based on the $\{Re_6S_i^i\}$ cluster core, we can note no modification of the Re contribution whereas the shape and the intensity of Cl, N, O, and C contributions are affected. Thus, a shoulder on the Cl 2p contribution appears at higher binding energy (around 200 eV) when the clusters are deposited on FTO substrates. This shoulder corresponds to another contribution of chlorine that has a more oxidized environment. It can be attributed to the modification of the chemical composition of the clusters during the EPD process. Indeed, a decrease of the Cl 2p peak intensity is observed

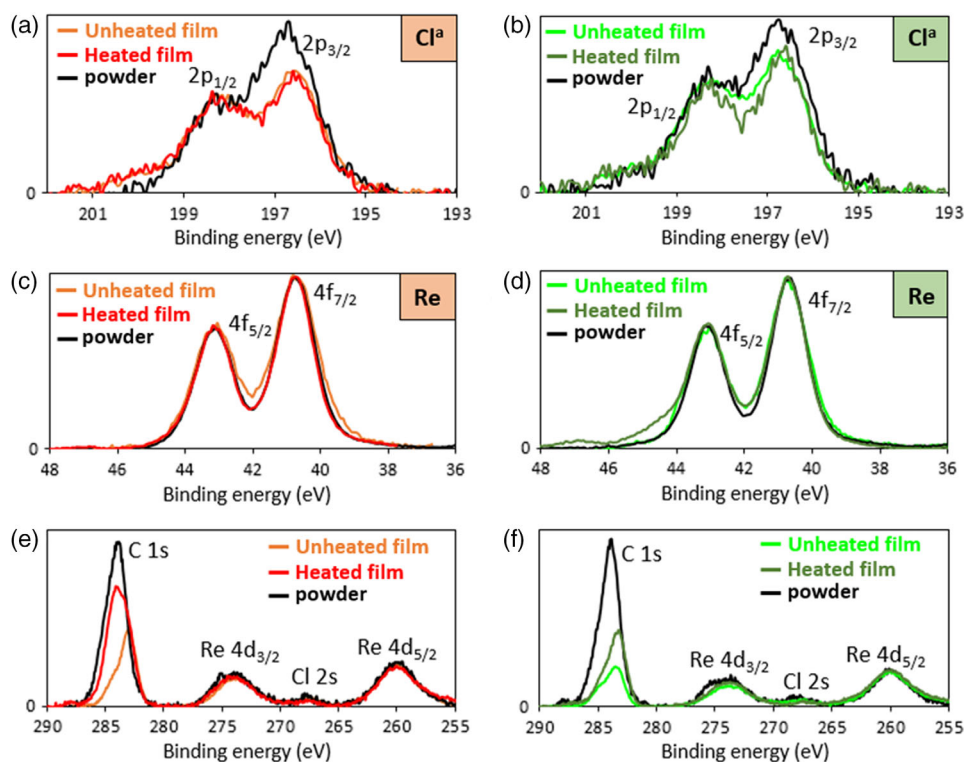


Figure 3. XPS spectra of a,b) the Cl 2p contribution, c,d) the Re 4f contribution, and e,f) the C 1s, the Re 4d, and the Cl 2s contributions of precursor powders, unheated and heated $\{Re_6Q_8\}$ -based films ($Q = S$ for (a), (c), and (e) spectra and $Q = Se$ for (b), and (d), (f) spectra). The intensity of the spectra was normalized.

Table 1. Atomic ratios calculated from the deconvolution of the Re 4f, Re 4d, and Cl 2p contributions.

Atomic ratios	$\{Re_6S_8\}$			$\{Re_6Se_8\}$		
	Powder	Film	Heated film	Powder	Film	Heated film
Re/Q ⁱ	0.73(5)	0.75(5)	0.66(5)	0.75(5)	0.79(5)	0.80(5)
Re/Cl ^a	0.93(8)	1.28(8)	1.14(8)	1.10(8)	1.20(8)	1.35(8)

after deposition, as a consequence of the increase in the ratio Re/Cl from 0.93(8) to 1.28(8) for the powder and for the film, respectively (Table 1, theoretical Re/Cl values equal to 1 for $(Bu_4N)_3\{[Re_6S_8]Cl_6\}$ and 1,2 for $(Bu_4N)_2\{[Re_6S_8]Cl_5(H_2O)\}$). This is concomitant with the increase of the oxygen contribution $(Re\ 4d + Re\ 4f)/(O\ 1s) = 3.7(2)$ and $3.1(2)$ for powder and film, respectively) and the decrease of the intensity of carbon and nitrogen peaks (for carbon: $(Re\ 4d)/(C\ 1s)$ ratio equals to 0.08(2) and 0.19(2) before and after deposition, respectively; for nitrogen: $(Re\ 4d)/(N\ 1s)$ ratio equals to 1.9(2) (theoretical value equals to 2 for $(n-C_4H_9)_4N_3\{[Re_6S_8]Cl_6\}$ and 2.9(2) (theoretical value equals to 3 for $(n-C_4H_9)_4N_2\{[Re_6S_8]Cl_5(H_2O)\}$) before and after deposition, respectively) (Figure 3e and S3, Supporting Information). This may be attributed to the substitution of one Cl apical ligand by one water molecule during the EPD process and to the concomitant loss of one Bu_4N^+ cation to keep the neutrality of the complex. The exchange of one apical Cl^- by a water molecule leads thus to a more oxidized local

environment that can correspond to the shoulder observed on the Cl 2p contribution discussed above. The presence of Cl exchanged and so partially oxidized on the top of the film can explain the new Cl 2p contribution too. By comparing the intensity of XPS peaks, one-thirds of apical chlorides are affected by the change of environment. This substitution of one chloride by a neutral water molecule leads to a decrease of the charge of the cluster units from 3- in the precursors based on $\{[Re_6S_8]Cl_6\}^{3-}$ to 2- for $\{[Re_6S_8]Cl_5(H_2O)\}^{2-}$. However, the valence electron concentration does not change with a constant value of 23. The estimated final composition of films based on $\{Re_6S_8\}$ cluster core is thus $((n-C_4H_9)_4N)_2\{[Re_6S_8]Cl_5(H_2O)^a\} \cdot xH_2O$.

The same tendency was observed for the $\{Re_6Se_8\}$ -based film. Briefly, a more oxidized contribution attributed to a modification of the formulae of the cluster unit increases on the chloride 2p peaks at higher binding energy (around 200 eV). Simultaneously, a decrease of the chloride 2p peaks intensity at 197 eV corresponding to the apical contribution is observed after deposition (Figure 3b and S4, Supporting Information). The Re/Cl ratio increases thus from 1.10(8) to 1.20(8) (theoretical Re/Cl value by equals to 1 for $(Bu_4N)_3\{[Re_6S_8]Cl_6\}$ and 1,2 for $(Bu_4N)_2\{[Re_6S_8]Cl_5(H_2O)^a\}$) (Table 1). This is concomitant with the increase of the oxygen contribution (the $(Re\ 4d + 4f)/(O\ 1s)$ ratios calculated equal to 1.8(2) and 5.0(2) for the powder and the film, respectively) and the decrease of nitrogen and carbon peak intensity (for carbon: $(Re\ 4d)/(C\ 1s)$ ratios equal to 0.07(2) and 2.3(1) before and after deposition, respectively; for

nitrogen: (Re 4d)/(N 1s) ratios equal to 2.4(2) (theoretical value = 2 for $(\text{Bu}_4\text{N})_3\{\{\text{Re}_6\text{S}_8^i\}\text{Cl}_6^a\}$) and 3.0(2) (theoretical value = 3 for $(\text{Bu}_4\text{N})_2\{\{\text{Re}_6\text{S}_8^i\}\text{Cl}_5(\text{H}_2\text{O})^a\}$) before and after deposition, respectively). Finally, we observe the substitution of one terminal chloride ligand by one water molecule and the loss of one Bu_4N^+ cation. The proposed formula of the $\{\text{Re}_6\text{S}_8^i\}$ selenide layer is thus $(\text{n-C}_4\text{H}_9)_4\text{N}_2\{\{\text{Re}_6\text{S}_8^i\}\text{Cl}_5(\text{H}_2\text{O})^a\}\cdot x\text{H}_2\text{O}$. Once deposited on the FTO surface, the general formula is the same for the sulfide and the selenide $(\text{n-C}_4\text{H}_9)_4\text{N}_2\{\{\text{Re}_6\text{Q}_8^i\}\text{Cl}_5(\text{H}_2\text{O})^a\}\cdot x\text{H}_2\text{O}$ (Q = S or Se). However, the highest (Re 4d + 4f)/(O 1s) ratio for the selenide than for the sulfide may be explained by a higher water content for the selenide. A thicker layer is observed in the selenide case (i.e., the thickness is ≈ 4 and ≈ 7 μm for $\{\text{Re}_6\text{S}_8^i\}$ and $\{\text{Re}_6\text{Se}_8^i\}$ -based cluster films respectively, Figure 2a,b). It is attributed to the higher conductivity of the selenide-based deposited layer. Indeed, the sheet resistance (resistivity) of the selenide film (R_s equals to 1.5Ω corresponding to a resistivity ρ of $4.9 \Omega \text{ cm}$) measured by the Van der Pauw measurement method is lower than that of the sulfide layer ($R_s = 1.9 \Omega$ and $\rho = 5.9 \Omega \text{ cm}$).

2.2. Optical and Electronic Properties of $\{\text{Re}_6\text{Q}_8^i\}$

Going from the sulfide to the selenide homologous affects the optical properties (Figure 4, S5, S6, Supporting Information and Table S1, Supporting Information). Indeed, optical bandgaps obtained from reflectance measurements are 2.41 eV for $\{\text{Re}_6\text{S}_8^i\}$ -based films and 2.20 eV for $\{\text{Re}_6\text{Se}_8^i\}$ -based films (Figure 4c,d). As expected, a decrease in bandgap is observed by increasing the size (and decreasing the electronegativity) of the chalcogen atom. These values are relatively close to those measured by diffuse reflectance on powders (2.11 eV for

$\{\text{Re}_6\text{S}_8^i\}$ and 1.93 eV for $\{\text{Re}_6\text{Se}_8^i\}$) (Figure 4a,b). However, we can note that the absorption bands are broader for the films that drastically affects the color by deposition of $\{\text{Re}_6\text{Se}_8^i\}$ cluster cores on FTO substrate (Figure 4).

To go further, the electronic properties of $\{\text{Re}_6\text{Q}_8^i\}$ -based photoelectrodes were determined by electrochemical characterizations. Cluster-based films were thus integrated as working electrodes in a three-electrode electrochemical cell. Chronopotentiometry and current–potential curves under chopped illumination gathered in Figure 5 clearly highlight the photoresponse and the semiconducting character of $\{\text{Re}_6\text{Q}_8^i\}$ -based photoelectrodes. These transient electrochemical characterizations point out divergent electronic behaviors for $\{\text{Re}_6\text{S}_8^i\}$ - and $\{\text{Re}_6\text{Se}_8^i\}$ -based layers. The current–potential measured on the sulfide-based photoelectrode and sketched in Figure 5a brings out its ambipolar character. Indeed, as already reported for $\{\text{Mo}_6\text{I}_8^i\}$ -based photoelectrodes,^[19] a photocurrent inversion translating the inversion of the charge carrier type at the photoelectrode surface is observed. For low potentials, a photoreduction current is recorded when the electrochemical cell is illuminated, whereas photo-oxidation current is measured when the applied potential becomes higher than the reversal potential of 0.25 V versus Ag/AgCl. This behavior is not observed on the current–potential curve measured for the selenide-based photoelectrode where only photoreduction currents are generated, whatever the applied potential.

The reverse evolution of the open-circuit potential (OCP) with the illumination recorded on $\{\text{Re}_6\text{S}_8^i\}$ - and $\{\text{Re}_6\text{Se}_8^i\}$ -based photoelectrodes confirms the different electronic behaviors. Indeed, in general, a decrease (increase) of OCP under illumination indicates that holes (electrons) constitute the minority charge carriers and demonstrates the n-typeness (p-typeness) of the semiconductor. Thus, as observed in Mo_6 cluster layers,^[19] the transport in the ambipolar $\{\text{Re}_6\text{S}_8^i\}$ -based layer is dominated by electron

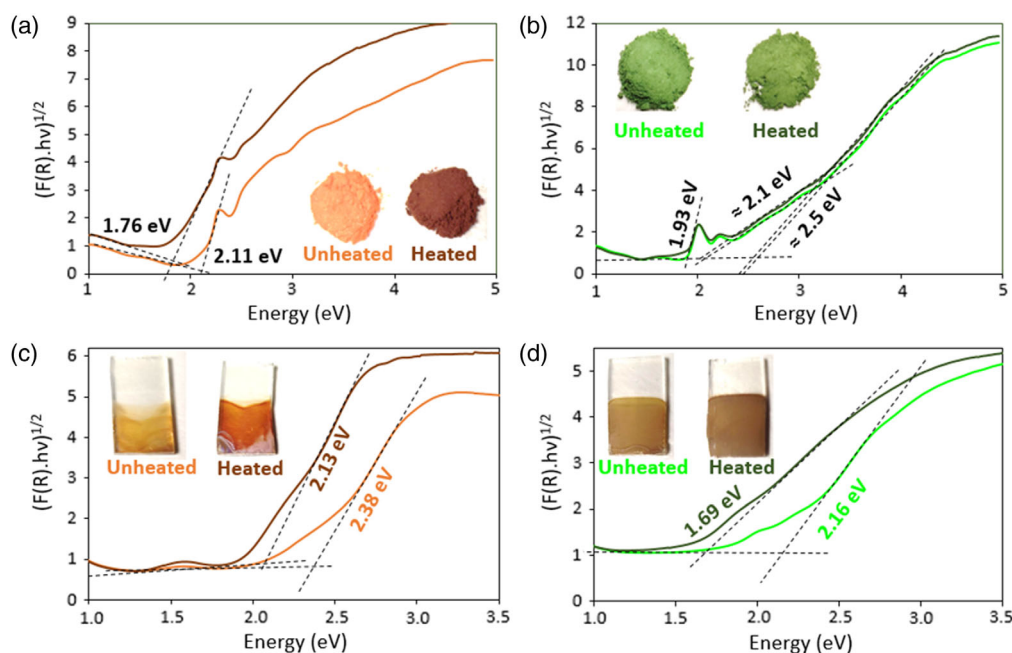


Figure 4. Tauc plots and corresponding photographs of unheated or heated precursor powders and films of Re_6 cluster a,c) sulfide and b,d) selenide.

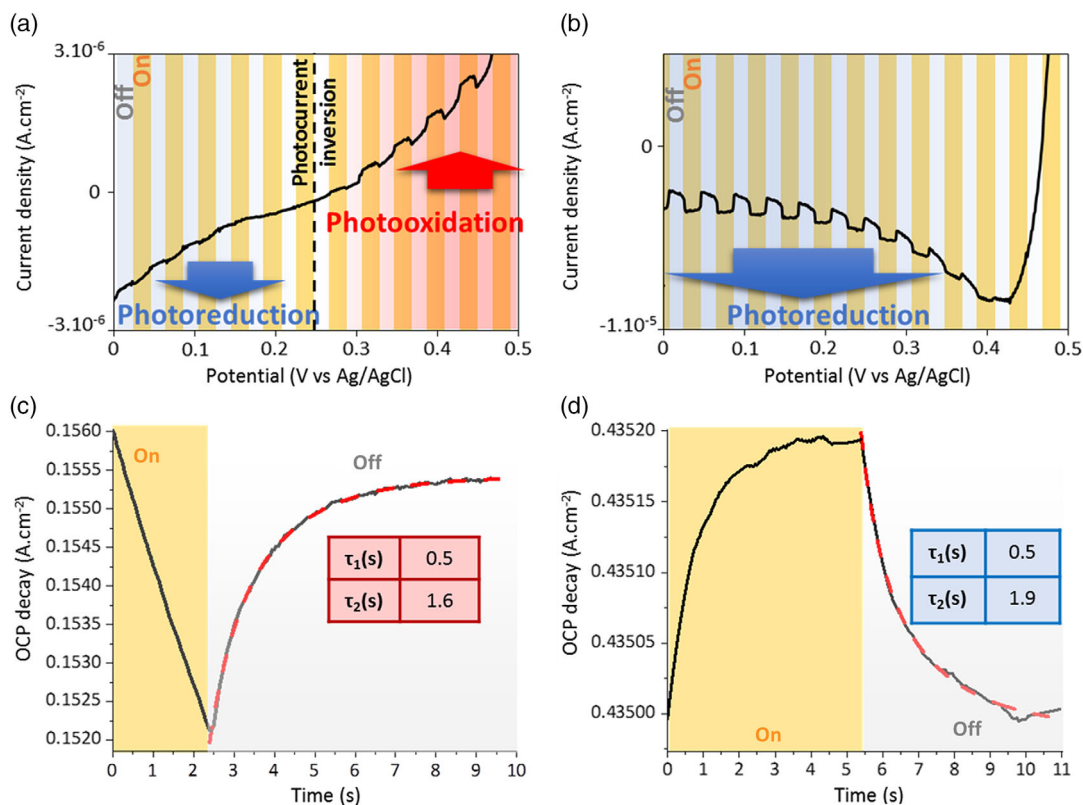


Figure 5. Polarization curves under chopped illumination for a) $\{\text{Re}_6\text{S}_8\}$ - and b) $\{\text{Re}_6\text{Se}_8\}$ -based films. Chronopotentiometry at OCP for c) $\{\text{Re}_6\text{S}_8\}$ - and d) $\{\text{Re}_6\text{Se}_8\}$ -based films.

transport (Figure 5c). This is consistent with the lower intensity of the photoreduction current compared to that of photooxidation current observed in current–potential curves (Figure 5a). In contrast, the $\{\text{Re}_6\text{Se}_8\}$ -based film appears clearly to be a p-type unipolar semiconducting layer (Figure 5b,d). Although the type of majority charge carrier in $\{\text{Re}_6\text{S}_8\}$ and $\{\text{Re}_6\text{Se}_8\}$ films is different, the lifetime of the photogenerated state determined by the OCP decay method (Figure 5c,d) after turning off the illumination is globally in the same value range.

In addition, electrochemical impedance spectroscopy measurements were carried out to determine the flatband potential and verify the majority charge carriers. The positive and negative slopes observed in the Mott–Schottky curves (Figure 6a,b) of $\{\text{Re}_6\text{S}_8\}$ - and $\{\text{Re}_6\text{Se}_8\}$ -based films, respectively, confirm the types of majority charge carriers for each layer (electron and hole for sulfide and selenide layer, respectively). Flatband potentials were determined for each cluster layer (0.64(3) and 0.98(3) V versus reversible hydrogen electrode [RHE] for $\{\text{Re}_6\text{S}_8\}$ - and $\{\text{Re}_6\text{Se}_8\}$ -based films respectively) and the Fermi-level location on an absolute energy scale with respect to the vacuum level was estimated (−5.14(3) and −5.48(3) eV for $\{\text{Re}_6\text{S}_8\}$ - and $\{\text{Re}_6\text{Se}_8\}$ -based films respectively) from the formulae E_{fb} (eV) = −4.5 − e · V_{fb} (RHE). Energy diagrams (Figure 7) were finally built from the position of Fermi levels, the valence band location (the difference $E_{\text{VB}} - E_{\text{F}}$ was estimated from XPS measurements, Figure S7, Supporting Information), and the value of optical bandgaps ($E_{\text{CB}} - E_{\text{VB}}$). Note here that the level of the top of

the valence obtained by XPS is in perfect agreement with that calculated from the reported value of the oxidized state $E_{\text{S}^{+}/\text{S}}$ measured by cyclic voltammetry (Figure S8, Supporting Information).^[37] That confirms the consistency of this method for energy-level determination.

The position of energy levels reflects the electronic properties observed earlier. The Fermi level of the selenide layers is located close to the top of its valence band as expected for a p-type semiconductor. In contrast, the Fermi level of the sulfide layer is positioned close to the middle of the bandgap and closer to the conduction band that clarifies the ambipolar behavior of $\{\text{Re}_6\text{S}_8\}$ -based semiconducting films dominated by electron transport. Electrical measurements highlighted the lower resistivity of selenide-based films that is coherent with the tendency reported by M. C. Kanadzidis on $\text{Re}_6\text{Q}_8\text{I}_2$ (Q = S, Se) semiconducting cluster compounds.^[40] Surprisingly, for the selenide compound, the carrier rate determined from the Mott–Schottky slope (Table 2) appears lower than that of the sulfide complex whereas its resistivity is lower. This can be attributed to higher charge carrier mobility or a different value of the permittivity for each compound. Indeed, to estimate the charge carrier density, we suppose a similar permittivity value for the selenide and the sulfide complexes.

These observed electronic behaviors were compared to those of the precursor compounds. Photoelectrodes based on dense pellets of powders were prepared by heating the pressed cluster-based precursor at 250 °C for 1 h under vacuum and

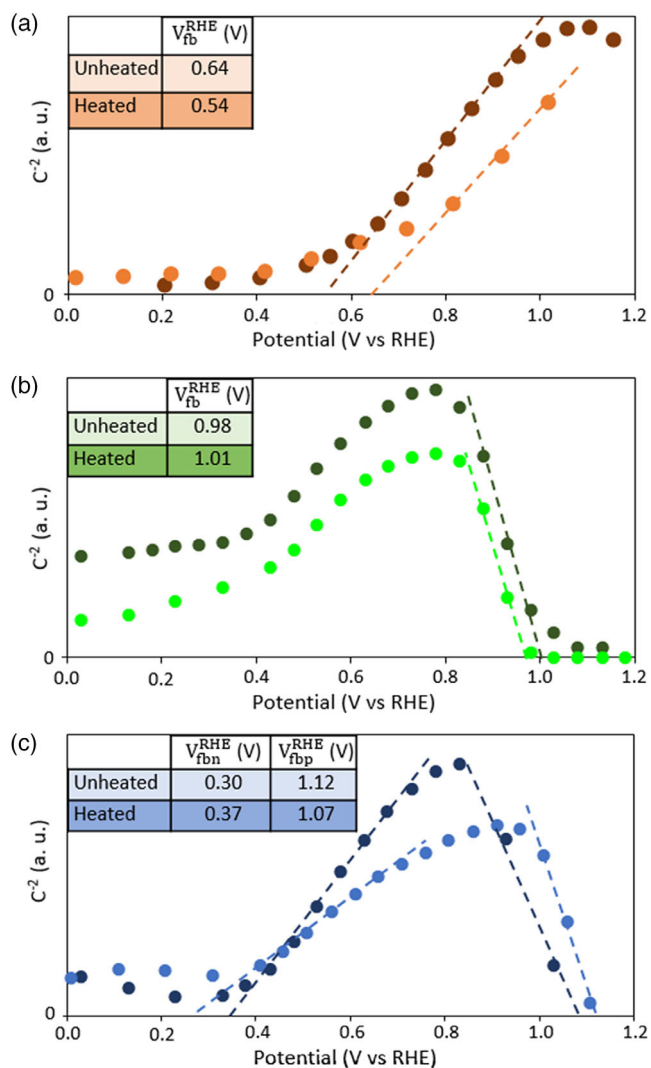


Figure 6. Mott-Schottky curves for a) $\{\text{Re}_6\text{S}_8\}$ -, b) $\{\text{Re}_6\text{Se}_8\}$ -, and c) mixed $\{\text{Re}_6\text{S}_8\}:\{\text{Re}_6\text{Se}_8\}$ (1:1)-based films. Unheated films are in light colors and heated films are in darker colors.

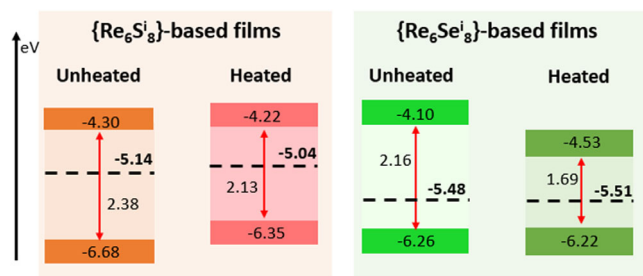


Figure 7. Energy diagrams calculated for unheated and heated at 200 °C $\{\text{Re}_6\text{S}_8\}$ -based films (orange) and unheated and heated at 200 °C $\{\text{Re}_6\text{Se}_8\}$ -based films (green). The error bars are 0.03 eV for the Fermi level and ± 0.05 eV for the valence and the conduction bands.

connecting them with copper wire in the backside. After fixing of the back contact with epoxy resin, the photoelectrodes were polished with silicon carbide papers. The conservation of the ratio

Re/Q (Q = S, Se) obtained by energy-dispersive spectroscopy (EDS) analyses before and after heating tends to demonstrate the preservation of the cluster unit composition. A redshift corresponding to a slight decrease of the optical bandgaps is, however, observed with the heating (Figure 4). This trend is attributed to an increase of interactions between the cluster units by removing water molecules trapped between them. The influence on the optical properties is stronger for the sulfide than the selenide powder. The electronic properties are globally similar than those determined on films. Even if a reverse potential is observed for the selenide-based pellet, the photoreduction currents are higher, suggesting a domination by the hole current (Figure S9, Supporting Information). For the sulfide electrode, as for films, an ambipolar behavior was highlighted. The determination of the types of majority charge carriers obtained by the Mott-Schottky method and the location of energy levels are in good agreement with those calculated on films too (Figure S8 and S10, Supporting Information). The electronic properties determined on films seem thus inherent to the cluster complexes and are not really impacted by the modification of the composition once deposited onto FTO substrates.

In order to reach higher photoresponses by increasing the conductivity of the photoelectrodes *via* the increase of the interactions between the building blocks, $\{\text{Re}_6\text{Q}_8\}$ -based films were also heated at 200 °C for 1 h. According to EDS analyses (for $\{\text{Re}_6\text{S}_8\}$ before and after heating, Re/S and Re/Cl ratios changed from 0.84(9) and 1.21(9) to 0.71(9) and 1.12(9); for $\{\text{Re}_6\text{Se}_8\}$, Re/Se and Re/Cl ratio changed from 0.76(9) and 1.20(9) to 0.80(9) and 1.22(9), respectively). Raman spectrometry (Figure S2, Supporting Information) and XPS spectra (Figure 3 and Table 1) show that the composition of the films is globally similar before and after heating. The number of chalcogenide and chlorine ligands is preserved (EDS and XPS data, Figure 3 and Table 1) and the cluster cores are not oxidized during the heating treatment. Indeed, no modification of the XPS peaks of Re 4d and Re 4f orbitals is observed on the sulfide-based film that conserves its Raman signature. For the selenide-based film, a new contribution appears on the Re 4f contribution around 45 eV ($4f_{7/2}$) and 47 eV ($4f_{5/2}$). However, due to its very low intensity, it is attributed to a slight oxidation of the surface. No Raman peaks were detected on the spectrum of the selenide film after heating because of its instability under the laser beam at 785 nm. A slight decrease of the Cl 2p contribution appeared at higher binding energy (200 eV) during the EPD process, which is however observed for both chalcogenides. It can be attributed to the removing of the free water molecules or the free exchanged Cl during the thermal treatment. The impact of heating on the optical and electronic properties of the films was investigated *via* the same set of optical, electrochemical, and spectroscopic characterizations used earlier. A decrease of the bandgaps and a slight shift of the flatband potentials corresponding to a shift of Fermi levels are concomitantly observed for both chalcogenide films (Figure 4, 6 and 7). Because of the stability of halide rhenium cluster complexes up to 200 °C during the heating process,^[41] the variation of their physical properties is attributed to the removing of water solvent molecules surrounding the clusters without modification of the ligand arrangement ($\{\{\text{Re}_6\text{S}_8\}\text{Cl}_5(\text{H}_2\text{O})^{\text{a}}\}$ and $\{\{\text{Re}_6\text{Se}_8\}\text{Cl}_5(\text{H}_2\text{O})^{\text{a}}\}$) within the cluster unit. The loss of water molecules induces a decrease of: 1) the distance

Table 2. Fermi levels, charge carrier densities, and photocurrents determined by the Mott–Schottky method.

	{Re ₆ S ₈ ⁱ }		{Re ₆ Se ₈ ⁱ }		Mixed films	
	Unheated film	Heated film	Unheated film	Heated film	Unheated film	Heated film
<i>E_{fb}</i> [eV]	−5.14	−5.04	−5.48	−5.51	−4.80/−5.62	−4.87/−5.57
<i>N</i> [cm ^{−3}]	4.10 ²⁰	2.10 ²⁰	9.10 ¹⁹	3.10 ¹⁹	4.10 ²⁰ /1.10 ²⁰	2.10 ²⁰ /9.10 ¹⁹
<i>I_{ph}</i> at 0 V versus Ag/AgCl [A cm ^{−2}]	1.4.10 ^{−7}	4.7.10 ^{−7}	9.8.10 ^{−7}	1.3.10 ^{−6}	5.1.10 ^{−6}	9.4.10 ^{−6}

between the cluster building blocks and 2) the thickness of the films. Indeed, as shown in Figure 2c,d, the thickness of the heated films was divided by 2 (to 4 μm to 2 μm before and after heating) and 3 (to 7 μm to 2.5 μm before and after heating) for {Re₆S₈ⁱ}- and {Re₆Se₈ⁱ}-based films, respectively. At the end, the density of clusters in the layers is increased and the physical properties of the films are impacted. Thus, the energy levels are impacted by the heating. Although the Fermi level tends to move closer to the conduction band for the sulfide and the valence band for the selenide, because of the shift of the flatband potentials (Figure S11, Supporting Information), the modification of the distance *E_F*–*E_{VB}* and the decrease of the bandgaps lead to an only slight modification of energy diagrams. For both chalcogenides, the Fermi level is finally slightly positioned more deeply in the bandgap (Figure 7 and Table 2). In other words, the Fermi level is closer to the middle of the bandgap. This leads to an exaltation of the ambipolar properties of the sulfide-based layer. The photoconductivity is thus improved (Figure S12a, Supporting Information and Table 2). Both photocurrents, photo-oxidation and photoreduction, are increased and they appear more stable. Similarly, the modification of the energy diagram of the selenide-based film by heating influences its electronic properties (Figure 7a, S12b, Supporting Information and Table 2). It leads to the appearance of a low photo-oxidation current at high potential for the selenide and the improvement of the photocurrents. However, the charge transport stays strongly dominated by the hole transport. We assume that the enhancement of the photoresponse of the films is due: 1) to the increase of the optical properties (improvement of the collection of photons by decreasing the bandgap) and especially 2) to the improvement of the intrinsic conductivity that causes a decrease of electron–hole recombinations. Because the number of charge carriers is not significantly affected by heating (Table 2), this better photoconductivity can be attributed to an increase of charge carrier mobility in the films.

2.3. p–n junction for {Re₆S₈ⁱ}: {Re₆Se₈ⁱ}

As {Re₆S₈ⁱ}- and {Re₆Se₈ⁱ}-based layers have opposite electronic properties (i.e., the charge transport is dominated by electrons and holes in sulfide and selenide films, respectively), we investigated the possibility to create p–n junctions in Re₆-based photoelectrodes by mixing sulfide and selenide clusters. The aim was to improve the photoresponse of the films by enhancing the separation of charge carriers because of the electric field induced by the micro-p–n ({Re₆Se₈ⁱ}-{Re₆S₈ⁱ}) junctions. Thus, films with various compositions in {Re₆S₈ⁱ} and {Re₆Se₈ⁱ} cluster cores were prepared by the simultaneous deposition of [{Re₆S₈ⁱ}

Cl^a₅(H₂O)^a]^{2−} and [{Re₆Se₈ⁱ}Cl^a₅(H₂O)^a]^{2−} by EPD process in the same conditions as previously described (i.e., using a voltage of 40 V for 30 s). Films were obtained from deposition of 0.01 M solutions composed of {Re₆S₈ⁱ}: {Re₆Se₈ⁱ} volume ratios of 1:1 and 3.7:1. The resulting {Re₆S₈ⁱ}: {Re₆Se₈ⁱ} ratios within the films were estimated to be equal to the S/Se measured by EDS analysis, that are, 0.3(1):1.0(1) and 1.6(1):1.0(1) respectively. By extrapolation, a film composed of a {Re₆S₈ⁱ}: {Re₆Se₈ⁱ} ratio of 1:1 was obtained from the mixture of the two [{Re₆S₈ⁱ}Cl^a₆]^{3−} and [{Re₆Se₈ⁱ}Cl^a₆]^{3−} precursor-based solutions (0.01 M) for a volume ratio of solution of 2.5:1 (Figure 8b). The morphology of the films is quite different by increasing the sulfide content (Figure 8a). For an atomic ratio of {Re₆S₈ⁱ}: {Re₆Se₈ⁱ} of 0.3:1, a porous film of around 4 μm of thickness composed of spherical particles with a diameter close to 500 nm is obtained (Figure S13, Supporting Information). The porosity and the thickness of the film decreases when the S/Se increases. The spherical particles appear such as those dispersed in a smoother matrix and the thickness falls to 3 and 1.5 μm for ratios of 1:1 and 1.6:1, respectively. The formation of particles is thus favored by the presence of selenide. The variation of morphology and composition impacts the photoresponse generated. Indeed, the photocurrent generated is higher for 1.6:1 than for 0.3:1 ratio and it is optimal for 1:1 (Figure 8c).

The optical and electronic properties of the mixed films were investigated. The absorption properties of the mixed {Re₆S₈ⁱ}: {Re₆Se₈ⁱ}-based cluster films associate the contributions of the sulfide and the selenide-based films with, however, an optical bandgap of 2.12(2) eV (Figure S14, Supporting Information), closer to that for the single-selenide-based film (2.20(2) eV). Moreover, the electronic properties of the mixed photoelectrodes seem to be controlled by the selenide units. Indeed, by mixing {Re₆S₈ⁱ} and {Re₆Se₈ⁱ} cluster cores, the p-type behavior prevails for all {Re₆S₈ⁱ}: {Re₆Se₈ⁱ} atomic ratios. A photoreduction current is recorded for each mixed photoelectrode and a negative slope attributed to the selenide part is observed in the Mott–Schottky plots of the mixed layers. Indeed, a pseudo-flatband *V_{fb}* of 1.12(3) V versus RHE (Figure 6) was determined at a potential value very close to that obtained for the single selenide-based film (0.98(3) V versus RHE). The mixture of the two cluster units influences, however, the physical properties of the mixed photoelectrodes. Thus, another slope at lower potential is observed too. It is more pronounced than the slight slope associated with the contribution of the FTO substrate for the {Re₆Se₈ⁱ} cluster-based single film and it matches another pseudo-flatband potential *V_{fb}* (0.30(3) V versus RHE) shift compared to that of the sulfide-based film (0.64(3) V versus RHE). All these experimental features translate the interactions between {Re₆S₈ⁱ} and {Re₆Se₈ⁱ} cluster cores and suggest the creation of a p–n heterojunction such

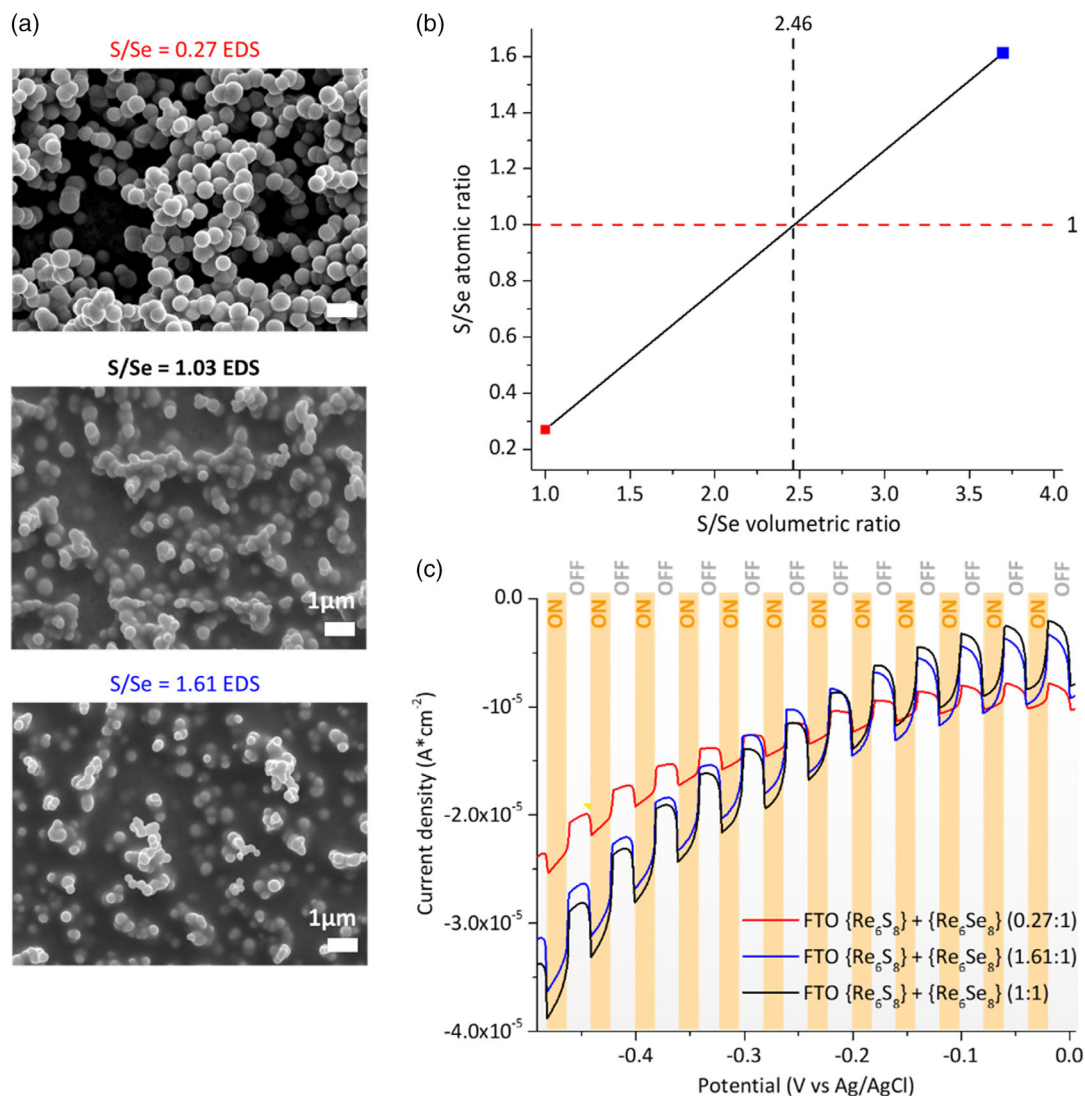


Figure 8. a) SEM images of mixed {Re₆S₈}³⁺:{Re₆Se₈}¹⁻-based films with various cluster (S/Se) ratios. b) Linear dependence between the volume ratios of the solutions and the atomic ratio determined by EDS for {Re₆S₈}³⁺:{Re₆Se₈}¹⁻ and c) polarization curves for corresponding mixed {Re₆S₈}³⁺:{Re₆Se₈}¹⁻-based films under chopped illumination.

observed in a type II heterostructure.^[42,43] Two pseudo-energy levels, corresponding to the flatband potential $V_{fb,n}$ and $V_{fb,p}$, are thus introduced in the energy diagram of the heterostructure. Due to the difference between these energy level values (difference in work functions), a band bending should occur after the equilibrium of the Fermi levels. This band bending appears higher in the sulfide side due to the higher difference between the Fermi level of the single film and the pseudo-energy level corresponding to $V_{fb,n}$ in the heterostructure. Microelectric fields are generated between the two cluster-based particles, which facilitate the separation of the photogenerated electron-hole pairs. It results in an improvement of the photoconductivity properties of the cluster-based films by mixing the two types of chalcogenides. Indeed, the intensity of the generated photocurrent is much higher (multiplied by a factor 10) than the photocurrents recorded for photoelectrodes

based on a single type of chalcogenide cluster (Figure 9 and Table 2).

The improvement of photocurrent is thus concomitant with an increase of the lifetime of the majority charge carriers in comparison with films based on selenide or sulfide cluster units (Figure S15, Supporting Information). Much higher performances were reached by annealing the mixed {Re₆S₈}³⁺:{Re₆Se₈}¹⁻-based cluster film at 200 °C for 1 h (Figure 9). Thus, it appears that the simultaneous deposition of {Re₆S₈}³⁺ and {Re₆Se₈}¹⁻ cluster cores favors the charge transport in photoelectrodes by creating micro-p-n junctions. The recombination of charge carriers is so limited (increase of the majority charge carrier lifetime) which leads to increased photocurrent values.

Many integrated nanostructured systems for sustainable energy conversion are reported and reviewed in the literature.^[42] They were classified according to their dimensionality from 0D

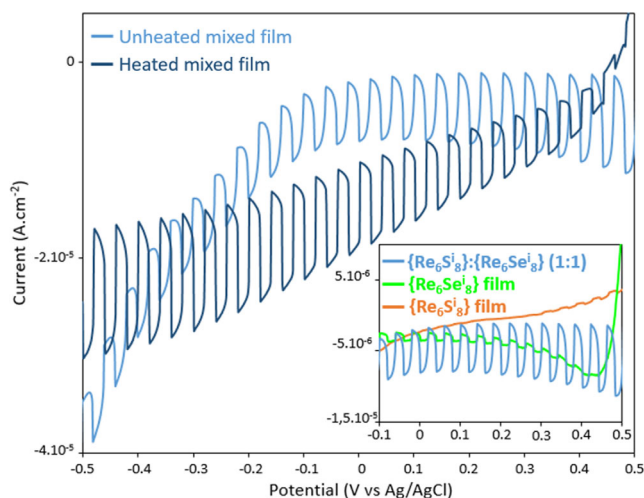


Figure 9. Polarization curves under chopped illumination of the unheated and the heated $\{\text{Re}_6\text{S}_8\}^i:\{\text{Re}_6\text{Se}_8\}^i$ -based films (1:1) and in inset the comparison with single films composed of $\{\text{Re}_6\text{S}_8\}^i$ or $\{\text{Re}_6\text{Se}_8\}^i$ cluster cores.

(QD), 1D (e.g., nanowires, nanorods...), 2D (nanosheets), to 3D (e.g., inverse opal structures).^[42] At first glance, $\{[\text{M}_6\text{L}_8^i]\text{L}'^a\}_6$ building blocks ($\text{M} = \text{Mo}, \text{Re}, \text{L} = \text{S}, \text{Se}$ or $\text{I}, \text{L}' = \text{Cl}, \text{H}_2\text{O}$ or I) could be compared to 0D nano-objects like QDs (e.g., CdSe or PbSe) with an energy bandgap favorable to the solar light harvesting.^[42] However, metal atom clusters are much better defined nanoscale objects than QDs since they are based on a precise number of metal atoms and ligands. Their properties (e.g., redox, absorption, and emission) can be efficiently optimized by combining solid-state and solution chemistry. For instance, in the case of $\{[\text{Mo}_6\text{X}_8^i]\text{X}'^a\}_6$ series (X and $\text{X}' = \text{Cl}, \text{Br}$ and I), the redox, absorption, and emission properties can be efficiently tuned by the judicious choice of X in capping position and X' in terminal position.^[44] The same type of optimization can be obtained for $\{[\text{Re}_6\text{Q}_8^i]\text{X}'^a\}_6$ cluster-based compounds by playing on the nature of face-capping ligand.^[34–39] Thus, compared to QDs, it can be pointed out that the added values of $\{[\text{M}_6\text{L}_8^i]\text{L}'^a\}_6$ ($\text{M} = \text{Mo}, \text{Re}, \text{L} = \text{S}, \text{Se}$ or $\text{I}, \text{L}' = \text{Cl}, \text{Br}, \text{I}$ or H_2O) building blocks are that: 1) they are based on atom-precise composition; 2) they do not contain toxic elements; 3) they are not submitted to surface defects that could alter their properties; and 4) their properties can be efficiently tuned by chemical engineering by the judicious choice of the metal, capping ligands, and terminal ligands. The solubilization of cluster-based solid-state precursors and the immobilization process onto semiconducting surfaces do not significantly alter the chemical formula of the building blocks that bears similar properties as those found in bulk compounds. This is a fundamental difference with nanoparticles of semiconducting sulfides, selenides, or oxides.^[42,45] Indeed, for the latter, a very fine control of the syntheses pathways to control the size of the nanoparticles is mandatory to obtain reproducible chemical and physical properties of nanoparticles with a minimum of surface defects.^[45] Because such problems are not faced with $\{[\text{M}_6\text{L}_8^i]\text{L}'^a\}_6$, they can be used in the design of photoelectrodes because high-quality interfaces are obtained not only between building blocks but also between

the building blocks and the semiconducting surfaces. Depending on the chemical nature of $\{[\text{M}_6\text{L}_8^i]\text{L}'^a\}_6$ building blocks, tuned photoelectrodes of p-type, n-type, or exhibiting an ambipolar behavior can be designed. To our knowledge, this has hitherto never been demonstrated for any other chemical system. Moreover, as shown herein, mixing $\{[\text{M}_6\text{L}_8^i]\text{L}'^a\}_6$ building blocks of different chemical compositions and exhibiting different physical properties (i.e., light absorption, redox potential, charge separation) enables to obtain nanocomposite layers with enhanced properties compared to those built on a single type of building block. It has also been shown that nanoheterojunction semiconductors/semiconductors of type II are built between two types of building blocks (i.e., $\{[\text{Re}_6\text{S}_8^i]\text{Cl}^a_5(\text{H}_2\text{O})^{a_1}2^-\}$ and $\{[\text{Re}_6\text{Se}_8^i]\text{Cl}^a_5(\text{H}_2\text{O})^{a_2}2^-\}$), leading to bending phenomenon. We hypothesize that numerous heterojunctions are formed at all the interfaces between immobilized building blocks $\{[\text{Re}_6\text{S}_8^i]\text{Cl}^a_5(\text{H}_2\text{O})^{a_1}2^-\}$ and $\{[\text{Re}_6\text{Se}_8^i]\text{Cl}^a_5(\text{H}_2\text{O})^{a_2}2^-\}$. It is supposed that the small size, the regular shape, and the absence of surface defects of the latter enable to maximize the number of local heterojunctions in the three directions of the space in a homogeneous way within the layers and with high quality of the p–n interfaces. The problem of interfaces between semiconducting nanoparticles of different natures in nanostructured systems is a well-known problem.^[45] Interfaces of low quality lead to the trapping of photogenerated holes and electrons and their recombination. Examples of these semiconductor/semiconductor nanostructured systems used for energy conversion are $\text{Cu}_2\text{O}/\text{TiO}_2$, NiO/TiO_2 , $\text{Co}_3\text{O}_4/\text{ZnO}$.^[45] Last but not least, the fact that cluster-based building blocks are soluble enables to simplify the integration processes using a simple and unique mode of immobilization from solutions containing either a single type of building block or a mixture of building blocks. This is particularly suited for immobilization by EPD or by recrystallization in the frame of nanoarchitectonics.

3. Conclusion

The concept of nanoarchitectonics to tailor the properties of photoelectrodes was extended from $\{\text{Mo}_6\text{I}_8\}$ to $\{\text{Re}_6\text{S}_8\}$ and $\{\text{Re}_6\text{Se}_8\}$ cluster-based building blocks. The investigation of photoelectrode properties of cluster-based layers versus their composition was deeply investigated. Re_6 chalcocyanide-based photoelectrodes were easily designed by the EPD deposition of $\{\text{Re}_6\text{S}_8\}^i$ and $\{\text{Re}_6\text{Se}_8\}^i$ cluster-based units onto FTO substrates. Hydrated and dehydrated active layers were successfully prepared. The impact of the composition on physical properties of the films was investigated through a set of optical, electrochemical, and spectroscopic characterization methods. It was highlighted that the optical and electronic properties are drastically dependent on the composition. The sulfide-based photoelectrodes exhibit ambipolar behavior with a slight domination of electron on the charge transport whereas the charge transport in selenide-based photoelectrodes is clearly dominated by the hole transport. Such electronic properties appear to be dependent on the interactions between the cluster building blocks. Indeed, the annealing of the films led to an increase in their intrinsic conductivity properties (increase of the interactions between the different building blocks) and allowed to improve the photoelectrode performances. It appears thus that the conductivity

properties of such photoelectrodes are improved by increasing the interaction between cluster building blocks and by increasing the density of the layers through simple heating at 200 °C. Beyond $\{Re_6S_8\}$ - and $\{Re_6Se_8\}$ - cluster-based photoelectrodes, we succeeded in tuning the electronic properties of photoelectrodes by designing active cluster-based layers by controlling the ratio between the two $\{Re_6S_8\}$ and $\{Re_6Se_8\}$ -based building blocks. We assume that the electric field created by the micro-(p-n) junctions formed by the interactions between the $\{Re_6Se_8\}$ - and $\{Re_6S_8\}$ -based clusters limits the recombination of charge carriers and consequently this leads to improving the photocurrent generated by such photoelectrodes. A ratio of 1:1 for $\{Re_6S_8\}:\{Re_6Se_8\}$ maximizes the number of local heterojunctions within the layers and allows to optimize photophysical properties. This study opens new perspectives in terms of nanoarchitectonics of cluster building blocks for the design of photoelectrodes dedicated to solar energy conversion. Indeed, the variety of compositions, structures, and possible interactions in cluster compounds offers huge possibilities to effectively tune the photoinduced conductivity properties of cluster-based photoelectrodes and optimize the sunlight conversion in solar fuels or in electrical energy. In view of the proof of concept already carried out on molybdenum iodide, the integration of such photoelectrodes in photoelectrocatalytic and photovoltaic systems is thus the essential next step to promote new alternative solar cells designed by nanoarchitectonics.

4. Experimental Section

Materials and Methods: All the reagents were purchased from commercial sources (Sigma-Aldrich, Fisher Chemical, Alfa Aesar, Acros) and were used as received without further purification.

Synthesis of $((n-C_4H_9)_4N)_3[Re_6S_8Cl_6]$ (1) and $((n-C_4H_9)_4N)_3[Re_6Se_8Cl_6]$ (2) Precursors: The compounds $K_4[Re_6Q_8(OH)_6] \cdot 8H_2O$ (Q = S, Se) were synthesized using a well-known technique.^[46] $((n-C_4H_9)_4N)_3[Re_6Q_8Cl_6]$ (Q = S, Se, Bu = $n-C_4H_9$) cluster complexes were obtained as a result of the reaction described earlier^[47] with several modifications. Briefly, $1.00 \times g$ of $K_4[Re_6Q_8(OH)_6]$ (0.56 mmol for Q = S and 0.46 mmol for Q = Se) was dissolved in 20 mL of H_2O . 30 mL of HCl (37 wt%, Sigma-Aldrich) was added to the solution and boiled for an hour. An excess of $(n-C_4H_9)_4NCl$ (1 g, 3.6 mmol) was then added to the stirring solutions and led to the formation of orange $((n-C_4H_9)_4N)_3[Re_6S_8]Cl_6$, named cluster sulfide precursor powder, or green $((n-C_4H_9)_4N)_3[Re_6Se_8]Cl_6$, named cluster selenide precursor powder precipitates, which were filtered and washed several times with H_2O .

Preparation of Photoelectrodes Based on $\{Re_6S_8\}$ and $\{Re_6Se_8\}$ Cluster Cores: $\{Re_6Q_8\}$ (Q = S, Se) cluster-based films were prepared by the following technique based on EPD method. Tetrabutylammonium salts of cluster complexes $((n-C_4H_9)_4N)_3[Re_6S_8]Cl_6$ and $((n-C_4H_9)_4N)_3[Re_6Se_8]Cl_6$ were dissolved in acetonitrile (HPLC grade, Fisher Chemical) (0.01 M). These deposition solutions were stocked and used for the following EPD process. Fluorine tin oxide (FTO) on glass was chosen as deposit substrate. Before deposition, FTO substrates were washed as previously described,^[19,48] according the following purification process carried out with step-by-step soaking in an ultra-sonication bath for 15 min: in 1) soapy water; 2) water with few drops of HCl_{conc} ; and 3) ethanol. A stainless-steel blade and an FTO substrate were used as cathode and anode, respectively. They were held face to face (1 cm of distance) by a carbon tape, connected to a Keithley Model 2450 Series SourceMeter, and placed into a cluster-based solution. The cluster deposition was carried out by applying a voltage of 40 V for 30 s. The obtained cluster-based films were then put into the deposition solution and dried in air at room temperature. Heated films were obtained by annealing at 200 °C for 1 h in air.

Preparation of Mixed Photoelectrode Based on $\{Re_6S_8\}:\{Re_6Se_8\}$ Cluster Cores: The preparations of mixed photoelectrodes based on $\{Re_6S_8\}$ and $\{Re_6Se_8\}$ were realized in similar conditions for the single photoelectrode. Films containing various ratios of $\{Re_6S_8\}:\{Re_6Se_8\}$ cluster cores (i.e., 0.3:1, 1:1, and 1.6:1) were prepared as described earlier from $(Bu_4N)_3[Re_6S_8]Cl_6$ and $(Bu_4N)_3[Re_6Se_8]Cl_6$ dissolved in acetonitrile with concentration 0.01M and mixed in volume ratio 1:1, 2.5:1, and 3.7:1, respectively.

Preparation of Cluster Precursor Pellet-Based Electrodes: $\{Re_6Q_8\}$ -based pellets were prepared by pressing powders of cluster precursors $(Bu_4N)_3[Re_6S_8]Cl_6$ (1) and $(Bu_4N)_3[Re_6Se_8]Cl_6$ (2). The pellets were then heated at 250 °C for 1 h in quartz tubes sealed under vacuum. They were then connected in the backside to a copper wire using carbon paste. The electrical contact was fixed by sealing with epoxy resin (CaldoFix-2kit, Struers). The cluster precursor pellet-based electrodes were finally polished with SiC papers (1200–4000 grids) to obtain smooth surfaces.

Characterization Techniques: The scanning microscopy images and EDS were obtained on a JEOL JSM 7100 F microscope operating at 10 kV with an energy-dispersive spectrometer. They were performed on pressed pellets of the cluster-based precursor powders and films on FTO both fixed on carbon tapes. The pellets were metallized with a gold coating whereas the films were contacted via the FTO substrate with a silver paste.

The powder X-ray diffraction patterns were collected at room temperature from 5° to 80° (2 θ) with a scan speed of 4° min⁻¹ with a Bruker D8 ADVANCE two-circle diffractometer (θ -2 θ Bragg-Brentano mode) using Cu K α radiation ($\lambda = 1.54056 \text{ \AA}$) equipped with a Ge(111) monochromator and a Lynx Eye detector.

The UV-vis-NIR diffuse reflectance spectra were obtained on a V-770 JASCO spectrophotometer using an integrated reflectance sphere accessory. The Kubelka Munk transforms were calculated from the reflectance values ($F(R) = (1-R)^2/2R$). The Tauc plots were calculated from the Kubelka Munk transform values according to the following formulae $(F(R).h\nu)^n$ with $n = 1/2$ and 2 for indirect and direct transitions, respectively.

XPS measurements were performed with an Mg K α (h ν) 1253.6 eV X-ray source measuring a VSW HA100 photoelectron spectrometer with a hemispherical photoelectron analyzer. The powder was directly deposited on a conductive copper tape. The films deposited on a glass were also fixed using copper tape and were contacted via the FTO substrate using a small silver drop that insured a good ground contact. By this way, no extra electron charge compensation was needed. All scans (wide spectra and resolved core level spectra) were recorded with a pass energy of 20 eV. The experimental resolution was 1.0 eV. Due to the presence of tetrabutylammonium in the compounds complexifying the C 1s contribution, binding energies of core levels were referenced to the Re 4d_{5/2} signal fixed at 260.0 eV.^[49,50] After a Shirley background subtraction, data were treated using Spectra PRESENTS program with mixed Gaussian-Lorentzian product. Re/Cl ratio was calculated from the intensity of Re 4f and Cl 2p peaks corrected by Scofield sensitivity factors. In Figure 3, the intensities of spectra were normalized to Cl 2p_{1/2}, Re 4f_{7/2}, and Re 4d_{5/2} respectively to highlight the differences.

The Raman scattering spectra were recorded using a LabRam Hight Resolution spectrometer coupled with a confocal microscope (Horiba Jobin Yvon), 600 g mm⁻¹ and 100 \times objective. A 785 nm laser diode was used for scattering excitation. Raman spectra were recorded at room temperature with 5 s exposition and two accumulations for powder $\{Re_6Q_8\}$ (Q = S, Se) cluster-based precursors and films. Spectra were recorded at different points of accumulation in order to check the homogeneity of the powders and the films.

The (photo)electrochemical measurements were performed on an Autolab PGSTAT204 (Metrohm AG) equipped with FRA32M electrochemical impedance spectroscopy module. The electrodes were illuminated using MI-LED illuminator source (Edmund Optics). For all measurements, a three-electrode electrochemical cell was used using a Pt auxiliary electrode and an Ag/AgCl reference electrode. The impedance spectra and the Mott-Schottky analyses were measured in a frequency range from 100 Hz to 100 kHz. The interface semiconductor/electrolyte capacitance (C) was determined using a simplified Randles equivalent circuit by neglecting the Warburg component at high frequency. The C values for

an applied potential were calculated from the constant phase element (CPE, $Z_{CPE} = 1/Q(j\omega)^\alpha$, $0 < \alpha < 1$), reflecting the nonideality of the interface capacitance using $C = (1/R_s + 1/R_{ct})^{(\alpha-1)/\alpha} Q^{1/\alpha}$ (with R_s and R_{ct} the series and the parallel charge transfer resistances, respectively). Flatband potentials (V_{fb}) were determined by extrapolation at $C^{-2} = 0$ from Mott–Schottky plots (C_{SC}^{-2} versus V) by assuming the approximation $C^{-2} \approx C_{SC}^{-2}$ and using the Mott–Schottky equation (Equation (1)) with a positive slope for n-type semiconductor and a negative slope for p-type semiconductor. Fermi levels were approximated on an absolute energy scale with respect to the vacuum level following the formulae E_{fb} (eV) = $-4.5 - e \cdot V_{fb}^{RHE}$ (RHE) with $V_{fb}^{RHE} = V_{fb}^{Ag/AgCl} + 0.199 + 0.06 \text{ pH}$ ($V_{fb}^{Ag/AgCl}$ is the potential imposed from Ag/AgCl reference). The error bar on the V_{fb}^{RHE} values and thus on E_{fb} (eV) values was estimated to 0.03 V. The charge carrier densities N were calculated for one order of magnitude that corresponded to the error bar

$$\frac{1}{C_{SC}^2} = \frac{2}{\epsilon \epsilon_0 e A^2 N} \left(V - V_{fb} - \frac{kT}{e} \right) \quad (1)$$

C_{SC} corresponds to the capacitance in the space–charge region of the semiconductor, A is the interfacial surface area between the semiconductor electrode and the electrolyte, k is the Boltzmann constant, T is the temperature, e is the electron charge, ϵ_0 is the vacuum permittivity, and ϵ is the relative permittivity of the semiconductor. C_{SC}^{-2} was approximated to be C^{-2} due to the large capacitance of the Helmholtz layer, at the semiconductor surface in the electrolyte, in comparison to C_{SC} .

The energy levels of precursor pellets and $\{Re_6Q_8\}$ -based films were estimated by combining complementary optical (UV–vis–NIR), spectroscopic (XPS), and electrochemical (cyclic voltammetry and impedance) techniques. The HOMO level was fixed from the Fermi level determined by the Mott–Schottky method using the difference between the valence band and the Fermi level measured by XPS. The LUMO level was then determined from the HOMO level according bandgap values ($E_g = E_{CB} - E_{VB} = E_{LUMO} - E_{HOMO}$). The error on the E_{VB} and E_{CB} values was estimated at ± 0.05 eV that corresponds to the error on the determination of the top of the valence obtained by XPS.

Supporting Information

Supporting Information is available from the Wiley Online Library or from the author.

Acknowledgements

T.L. and S.C. contributed equally to this work. The authors thank the CMEBA platform (Francis Gouttefangeas and Loic Joanny) from UMS 2001 ScanMAT CNRS-Université Rennes 1 for the FESEM images and analyses (Figure 2, 8, and 11). Raman investigations were performed using facilities available on SIR Platforms from UMS 2001 CNRS-Université Rennes 1 (Figure S2, Supporting Information). The authors are very grateful to Bertrand Lefeuvre ISCR UMR 6226 CNRS-Université Rennes1. The authors thank Rennes Metropole for its financial support via AIS funding.

Conflict of Interest

The authors declare no conflict of interest.

Data Availability Statement

The data that support the findings of this study are available in the supplementary material of this article.

Keywords

ambipolar properties, nanoarchitectonics, photoelectrodes, rhenium cluster building blocks, solar cell applications

Received: November 18, 2022

Revised: December 20, 2022

Published online:

- [1] G. Giorgi, K. Yamashita, *J. Mater. Chem. A* **2015**, *3*, 8981.
- [2] L. Chen, Y. Léger, G. Loget, M. Piriye, I. Jaldi, S. Tricot, T. Rohel, R. Bernard, A. Beck, J. Le Pouliquen, P. Turban, P. Schieffer, C. Levallois, B. Fabre, L. Pedesseau, J. Even, N. Bertru, C. Cornet, *Adv. Sci.* **2022**, *9*, 2101661.
- [3] M. Zhang, M. Ye, W. Wang, C. Ma, S. Wang, Q. Liu, T. Lian, J. Huang, Z. Lin, *Adv. Mater.* **2020**, *32*, 2000999.
- [4] Z. Wang, Q. Li, Y. Chen, B. Cui, Y. Li, F. Besenbacher, M. Dong, *NPG Asia Mater.* **2018**, *10*, 703.
- [5] Y. Zhou, S.-T. Han, P. Sonar, V. A. L. Roy, *Sci. Rep.* **2013**, *3*, 2319.
- [6] Y.-F. Lin, Y. Xu, S.-T. Wang, S.-L. Li, M. Yamamoto, A. Aparecido-Ferreira, W. Li, H. Sun, S. Nakaharai, W.-B. Jian, K. Ueno, K. Tsukagoshi, *Adv. Mater.* **2014**, *26*, 3263.
- [7] S. Z. Bisri, C. Piliago, J. Gao, M. A. Loi, *Adv. Mater.* **2014**, *26*, 1176.
- [8] Y. Ren, J.-Q. Yang, L. Zhou, J.-Y. Mao, S.-R. Zhang, Y. Zhou, S.-T. Han, *Adv. Funct. Mater.* **2018**, *28*, 1805599.
- [9] X. Chen, J. Pan, J. Fu, X. Zhu, C. Zhang, L. Zhou, Y. Wang, Z. Lv, Y. Zhou, S.-T. Han, *Adv. Electron. Mater.* **2018**, *4*, 1800444.
- [10] H. Kwon, H. Yoo, M. Nakano, K. Takimiya, J.-J. Kim, J. Kyu Kim, *RSC Adv.* **2020**, *10*, 1910.
- [11] A. Wannebroucq, S. Ouedraogo, R. Meunier-Prest, J.-M. Suisse, M. Bayo, M. Bouvet, *Sens. Actuators, B* **2018**, *258*, 657.
- [12] J. Zaumseil, R. H. Friend, H. Sirringhaus, *Nat. Mater.* **2006**, *5*, 69.
- [13] M.-H. An, R. Ding, Q.-C. Zhu, G.-D. Ye, H. Wang, M.-X. Du, S.-N. Chen, Y. Liu, M.-L. Xu, T. Xu, W. Wang, J. Feng, H.-B. Sun, *Adv. Funct. Mater.* **2020**, *30*, 2002422.
- [14] W. S. Bouree, M. S. Prevot, X. A. Jeanbourquin, N. Guijarro, M. Johnson, F. L. Formal, K. Sivula, *Adv. Mater.* **2016**, *28*, 9308.
- [15] B. Kim, M. L. Geier, M. C. Hersam, A. Dodabalapur, *Sci Rep* **2017**, *7*, 39627.
- [16] L. Portilla, J. Zhao, Y. Wang, L. Sun, F. Li, M. Robin, M. Wei, Z. Cui, L. G. Occhipinti, T. D. Anthopoulos, V. Pecunia, *ACS Nano* **2020**, *14*, 14036.
- [17] S. Fan, X. Tang, D. Zhang, X. Hu, J. Liu, L. Yang, J. Su, *Nanoscale* **2019**, *11*, 15359.
- [18] L. Zheng, W. Zhou, Z. Ning, G. Wang, X. Cheng, W. Hu, W. Zhou, Z. Liu, S. Yang, K. Xu, M. Luo, Y. Yu, *Adv. Opt. Mater.* **2018**, *6*, 1800985.
- [19] A. Renaud, P.-Y. Jouan, N. Dumait, S. Ababou-Girard, N. Barreau, T. Uchikochi, F. Grasset, S. Jobic, S. Cordier, *ACS Appl. Mater. Interfaces* **2022**, *14*, 1347.
- [20] S. Cordier, F. Grasset, Y. Molard, M. Amela-Cortes, R. Boukherroub, S. Ravaine, M. Mortier, N. Ohashi, N. Saito, H. Haneda, *J. Inorg. Organomet. Polym. Mater.* **2015**, *25*, 189.
- [21] N. T. K. Nguyen, C. Lebastard, M. Wilmet, N. Dumait, A. Renaud, S. Cordier, N. Ohashi, T. Uchikoshi, F. Grasset, *Sci. Technol. Adv. Mater.* **2022**, *23*, 547.
- [22] K. Ariga, *Nanoscale Horiz.* **2021**, *6*, 364.
- [23] S. Cordier, F. Dorson, F. Grasset, Y. Molard, B. Fabre, H. Haneda, T. Sasaki, M. Mortier, S. Ababou-Girard, C. Perrin, *J. Clust. Sci.* **2009**, *20*, 9.
- [24] S. Cordier, B. Fabre, Y. Molard, A. B. Fadjie-Djomkam, N. Tournerie, S. Ababou-Girard, A. Ledneva, N. G. Naumov, A. Moréac, C. Godet, *J. Phys. Chem. C* **2010**, *114*, 18622.
- [25] S. Cordier, B. Fabre, Y. Molard, A.-B. Fadjie-Djomkam, P. Turban, S. Tricot, S. Ababou-Girard, C. Godet, *J. Phys. Chem. C* **2016**, *120*, 2324.

- [26] M. Kepenekian, Y. Molard, K. Costuas, P. Lemoine, R. Gautier, S. A. Girard, B. Fabre, P. Turban, S. Cordier, *Mater. Horiz.* **2019**, 6, 1828.
- [27] T. K. N. Nguyen, A. Renaud, B. Dierre, B. Bouteille, M. Wilmet, M. Dubernet, N. Ohashi, F. Grasset, T. Uchikoshi, *Bull. Chem. Soc. Jpn.* **2018**, 91, 1763.
- [28] T. K. N. Nguyen, N. Dumait, F. Grasset, S. Cordier, D. Berthebaud, Y. Matsui, N. Ohashi, T. Uchikoshi, *ACS Appl. Mater. Interfaces* **2020**, 12, 40495.
- [29] T. K. N. Nguyen, K. Harada, F. Grasset, C. Comby-Zerbino, L. MacAleese, F. Chiro, P. Dugourd, N. Dumait, S. Cordier, N. Ohashi, M. Matsuda, T. Uchikoshi, *NPG Asia* **2022**, 14, 21.
- [30] P. Kumar, H. P. Mungse, S. Cordier, R. Boukherroub, O. P. Khatri, S. L. Jain, *Carbon* **2015**, 94, 91.
- [31] P. Kumar, S. Kumar, S. Cordier, S. Paofai, R. Boukherroub, S. L. Jain, *RSC Adv.* **2014**, 4, 10420.
- [32] M. Feliz, P. Atienzar, M. Amela-Cortes, N. Dumait, P. Lemoine, Y. Molard, S. Cordier, *Inorg. Chem.* **2019**, 58, 15443.
- [33] M. Feliz, M. Puche, P. Atienzar, P. Concepción, S. Cordier, Y. Molard, *ChemSusChem* **2016**, 9, 1963.
- [34] T. G. Gray, C. M. Rudzinski, E. E. Meyer, D. G. Nocera, *J. Phys. Chem. A* **2004**, 108, 3238.
- [35] T. G. Gray, C. M. Rudzinski, E. E. Meyer, R. H. Holm, D. G. Nocera, *J. Am. Chem. Soc.* **2003**, 125, 4755.
- [36] W. A. Rabanal-León, J. A. Murillo-López, D. Páez-Hernández, R. Arratia-Pérez, *J. Phys. Chem. A* **2014**, 118, 11083.
- [37] J.-C. P. Gabriel, K. Boubekeur, S. Uriel, P. Batail, *Chem. Rev.* **2001**, 101, 2037.
- [38] Z. P. Zheng, T. G. Gray, R. H. Holm, *Inorg. Chem.* **1999**, 38, 4888.
- [39] J. R. Long, L. S. Mac Carty, R. H. Holm, *J. Am. Chem. Soc.* **1996**, 118, 4603.
- [40] C. C. Laing, J. Shen, D. G. Chica, S. A. Cuthriell, R. D. Schaller, C. Wolverton, M. G. Kanatzidis, *Chem. Mater.* **2021**, 33, 5780.
- [41] V. Logvinenko, V. Fedorov, Y. Mironov, V. Drebushchak, *J. Therm. Anal. Calorim.* **2007**, 88, 687.
- [42] H. Lu, J. Tournet, K. Dastafkan, Y. Liu, Y. H. Ng, S. K. Karuturi, C. Zhao, Z. Yin, *Chem. Rev.* **2021**, 121, 10271.
- [43] G. Swain, S. Sultana, J. Moma, K. Parida, *Inorg. Chem.* **2018**, 57, 10059.
- [44] S. Akagi, S. Fujii, N. Kitamura, *Dalton Trans.* **2018**, 47, 113.
- [45] C. Xu, P. R. Anusuyadevi, C. Aymonier, R. Luque, S. Marre, *Chem. Soc. Rev.* **2019**, 48, 3868.
- [46] S. S. Yarovoi, Y. V. Mironov, D. Y. Naumov, Y. V. Gatilov, S. G. Kozlova, S.-J. Kim, V. E. Fedorov, *Eur. J. Inorg. Chem.* **2005**, 2005, 3945.
- [47] L. R. Long, L. C. McCarty, R. H. Holm, *J. Am. Chem. Soc.* **1996**, 118, 4603.
- [48] A. Renaud, T. K. N. Nguyen, F. Grasset, M. Raissi, V. Guillon, F. Delabrouille, N. Dumait, P.-Y. Jouan, L. Cario, S. Jobic, Y. Pellegrin, F. Odobel, S. Cordier, T. Uchikoshi, *Electrochim. Acta* **2019**, 317, 737.
- [49] C. D. Wagner, A. V. Naumkin, A. Kraut-Vass, J. W. Allison, C. J. Powell, J. R. Jr. Rumble, <http://srdata.nist.gov/xps/> (accessed: August 2003).
- [50] B. Vincent Crist, *The Elements and Native Oxides*, John Wiley and Sons, Hoboken, NJ, United States **2000**.